Supporting Information to:

Magnesium-vacancy optical centers in diamond

Emilio Corte, Greta Andrini, Elena Nieto Hernández, Vanna Pugliese, Ângelo Costa, Goele Magchiels, Janni Moens, Shandirai Malven Tunhuma, Renan Villarreal, Lino M.C. Pereira, André Vantomme, João Guilherme Correia, Ettore Bernardi, Paolo Traina, Ivo Pietro Degiovanni, Ekaterina Moreva, Marco Genovese, Sviatoslav Ditalia Tchernij, Paolo Olivero, Ulrich Wahl, Jacopo Forneris

Note: numbers of references are with respect to those in the main paper

1. Schematic illustration of the emission channeling technique

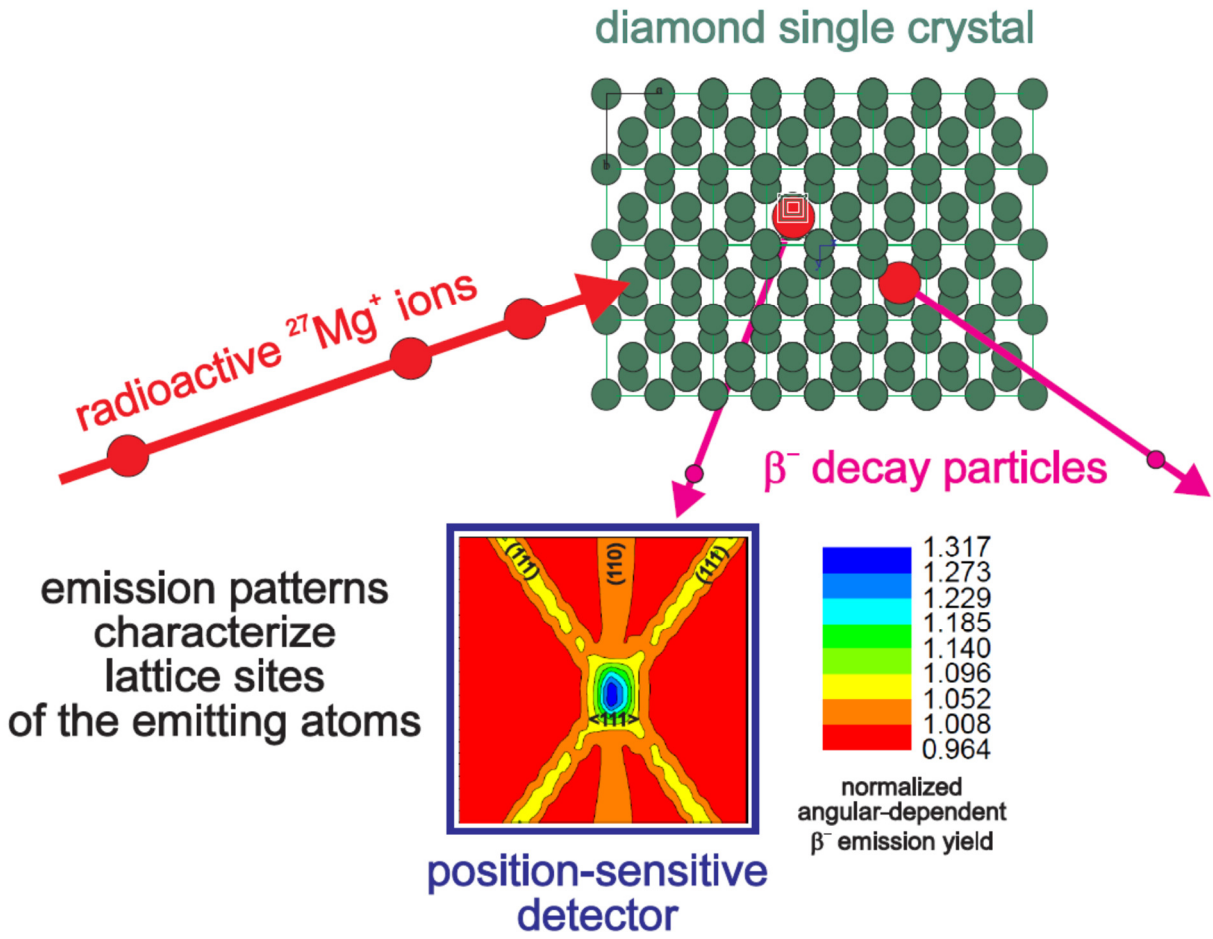

Figure S1. Schematic illustration of the emission channeling method [27-30]. Radioactive ^{27}Mg probe atoms are implanted into diamond single crystals. A position-sensitive Si detector (PSD, 3×3 cm^2 size at distance of 30 cm [29]) is used to detect emitted β^- particles in the vicinity of major crystallographic directions. Depending on the lattice site of the ^{27}Mg atoms, emitted β^- particles are channeled or blocked on their way out of the crystal. In this example, the diamond crystal is shown oriented along a <110> direction, with two incorporated Mg impurities, one (left) on a bond-center (BC) site within a double vacancy, and another (right) on a substitutional (*S*) site. Note that, while for the sake of clarity, the implanted Mg atoms in these examples are shown in the first few layers, typical implantation depths are ~278(94) Å, hence the channeling effects of the outgoing β^- particles are subject to coherent scattering from hundreds of aligned layers of C atoms. The angular-dependent emission rate measured by means of the PSD (with the scale indicated by the colour bar in the figure) consists of a linear superposition of the emission patterns from the different types of lattice sites. As an example, the shown 2D pattern represents the measured superposition of 15% S, 42% BC, and 43% random sites, with the orientation of the <110> pattern reflecting the orientation of the crystal as shown schematically by the lattice in the picture. While the central, blue spot represents higher electron count rate (normalized yield up to ~1.317) due to channeling along the axial <110> direction, also some of the major planes such as (111) and (110) can be seen in orange or yellow with count rates above normal due to planar channeling effects. The intensity of axial and planar effects strongly varies with the type of lattice site, as is indicated below in section 5.

2. Additional info on Emission Channeling (EC) experimental parameters and data analysis

^{27}Mg ($t_{1/2}$=9.45 min) was produced at CERN's ISOLDE on-line isotope separator facility by means of bombarding a Ti target with 1.4 GeV protons, thus causing nuclear fragmentation reactions. Following out-diffusion from the ~2000°C hot target, Mg atoms were selectively ionized to Mg^+ by means of resonant laser ionization, followed by 30 kV electrostatic acceleration and separation of mass 27 using the ISOLDE General Purpose Separator (GPS) 90° magnet ($M/\Delta M$~2400). More details on the production of ^{27}Mg with specific references to the literature can be found in our previous publications [32,33]. The implanted beam consisted of a mixture of radioactive ^{27}Mg with a small contamination of stable ^{27}Al. The contamination of ^{27}Al cannot be avoided, since this stable isotope is also produced by the proton beam fragmentation reactions in the target, diffuses slowly out of the Ti target and is ionized on hot metal surfaces of the ion source, although less efficient than the laser ionization process of Mg. However, the content of ^{27}Al was minimized by the following procedures:

- Mg is only ionized by means of the Resonant Laser Ionization (RILIS) process but not by surface ionization. Hence, measuring the ion beam current with lasers deactivated allows determining the Al content of the beam.
- The temperatures of the target (regulating out-diffusion of Mg and Al) and of the ion source (regulating ionization of Al on hot surfaces *vs* possible neutralization of Mg^+) were optimized thus as to maximize $^{27}Mg^+$ *vs* $^{27}Al^+$ yields, which resulted in ^{27}Al / (^{27}Mg+^{27}Al) = 1.6%.
- Gating of the ion beam for 1 second after impact of the pulsed proton beam on the Ti target (mean proton beam repetition time 3.5 s) allowed suppressing ^{27}Al further by a factor of 3-4. This is due to the fact that Al continuously but slowly (on a time scale of hours) diffuses out of the target, while Mg is subject to fast diffusion and hence is released from the target in bunches of less than a second duration only.

We note that, in any case, stable ^{27}Al will accumulate in the sample during the course of the EC experiments since it is the radioactive decay product of ^{27}Mg. The above-described measures hence serve the purpose of avoiding implanting the sample with stable atoms that would create additional damage but not contribute to measuring the lattice location of Mg.

The position-sensitive Si pad detector used for the experiments has been described in detail in Ref. [29]. It consists of 22×22 pixels of 1.3×1.3 mm^2 size and was placed at a distance of 301 mm from the sample. As is outlined in Ref. [29], for this geometry the overall angular resolution of the measurements resulting from the size of the detector pixels and the dimension of the 1 mm diameter beam spot on the sample was around 0.1° (standard deviation) for an angular range of ±2.7°.
The total number of events (i.e. particles detected) and resulting average number of events per pixel for each of the measured patterns is given in the following table.

Table S1: Total number of events and average events/pixel for each pattern shown in **Figures 1 and 2** of the main paper.

Figure	Channeling axis	Implantation temperature	Total number of events	Average events/pixel
1a	<110>	RT	1858226	3839
1b	<211>	RT	3111907	6430
1c	<100>	RT	1917060	3961
1d	<111>	RT	2639527	5454
2a	<110>	800°C	1400387	2893
2b	<211>	800°C	1218237	2517
2c	<100>	800°C	1506727	3113
2d	<111>	800°C	2078887	4295

The fit procedures in order to determine the normalization and exact orientation of the patterns, and to identify and quantify the occupied lattice sites were performed as described in Ref. [34] using our proprietary software FDD.
The display of the normalized angular-dependent electron count rate in **Figures 1 and 2** of the main paper shows contour plots produced from the 22×22 pixel matrices using the graphical software Origin 8.0. This type of representation is used for display purposes, in the same manner as we have used in all our previous publications for emission channeling patterns measured with a pad detector. It has the advantage of revealing considerably more details to the human eye than simple matrix plots.

3. Implementation of "many-beam" simulations for the diamond structure

In order to quantitatively analyze the experimental electron emission distributions, they were fitted by theoretical emission patterns for various lattice sites, which were calculated using the "many-beam" formalism for electron channeling [27,28]. The many-beam formalism is considered a standard tool in simulating electron diffraction phenomena in periodic structures and finds widespread applications, e.g. in electron microscopy or Reflection High Energy Electron Diffraction (RHEED). More

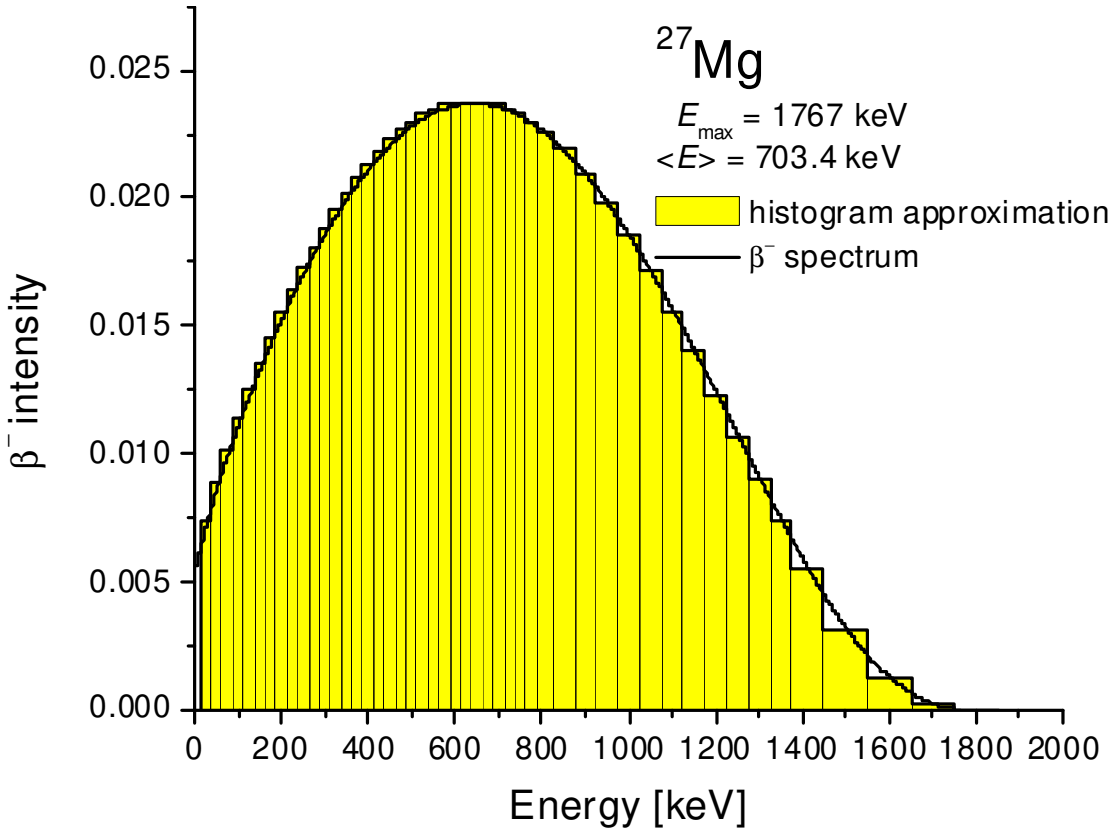

Figure S2. Histogram of the energy values used to approximate the β⁻ spectrum of ^{27}Mg in the "many-beam" calculations.

information regarding the application of the many-beam formalism to diamond with references to original literature can be found in the Supplemental Material to Ref. [31].

Due to the fact that the movement of electrons inside a crystal is subject to diffraction, their trajectories are not well described by the laws of classical mechanics but require a quantum mechanical treatment. Moreover, typical energies of β particles from nuclear decay may reach up to several MeV, hence demanding a relativistic description. Both aspects are combined using the many-beam diffraction theory of electron channeling in single crystals. In these calculations, the crystal potential is approximated by a superposition of atomic Doyle-Turner (DT) potentials. The DT potentials result from Hartree-Fock calculations and are parametrized as exponentially screened potentials, in order to make them especially suited for Fourier methods. Since for a description of the channeling effect only electrons moving under relatively small angles with respect to the channeling axis are relevant and these move at relativistic velocities, the potential along the channeling direction can be averaged ("continuum potential") and the electron wave function split into a longitudinal component along the channeling direction, which obeys a relativistic Klein-Gordon equation, and a transverse component perpendicular to the axis, which is given by the solution of a two-dimensional Schrödinger equation in a periodic potential. The β⁻ particle flux density inside the crystal can then be calculated after obtaining the transverse electron wave function using standard Fourier decomposition and Bloch wave techniques. The many-beam approach has proven to accurately describe EC effects in a multitude of cases, as has been demonstrated many times, e.g. in Refs [29,31-34], or as reviewed in Refs [27,28,30].

For diamond, the crystal potential was approximated by a superposition of atomic potentials calculated in the Doyle-Turner representation, using the sets of five coefficients a_i and b_i for carbon (a_i = 0.6617, 1.193, 0.4899, 0.1316, 0.03083, b_i = 38.88, 12.27, 3.311, 0.6327, 0.07613). To account for the continuous β⁻ spectrum of ^{27}Mg, many-beam simulations were performed for a number of discrete electron energies (step widths of 25 keV in the energy range 25-800 keV, 50 keV in the range 800-1400 keV, 100 keV in the range 1400-1800 keV, and weighting as indicated by the histogram according to the β⁻ spectrum of ^{27}Mg (**Figure S2**). The number of "beams" used in the simulations which defines the number of Fourier components for the crystal potential and for the transverse periodic part of the electron Bloch wave functions, can be found in **Table S2**. Angular patterns were calculated in x- and y-direction from −3° to +3° in steps of 0.05°. Structural parameters of the diamond used in the calculations were the lattice constant a = 3.567 Å and the room temperature (RT) root mean square (rms) displacement of carbon atoms u_1(C) = 0.0435 Å at 293 K, corresponding to a Debye temperature of 1860 K. Assuming that the Debye temperature of ^{27}Mg on substitutional C sites scales according to $T_D(^{27}\text{Mg}) = T_D(^{12}\text{C})[12/27]^{1/2}$ = 1240 K, this leads to an expected value of $u_1(^{27}\text{Mg})$ = 0.0383 Å that is somewhat lower than $u_1(^{12}\text{C})$. While 0.038 Å was used as default rms impurity displacement in the many-beam calculations for all sites, for the S and BC sites we also calculated theoretical patterns for rms displacements up to 0.5 Å in steps of 0.01 Å.

Table S2. Number of "beams" n and corresponding numbers of Fourier components used in the many-beam electron channeling simulations.

Crystal axis	Energy range [keV]	Number of "beams" n	Number of Fourier components of continuum potential $(2n+1)^2$	Number of Fourier components of electron wave functions $(n+1)^2$
<110>	25-750	16	1089	289
	775-950	20	1681	441
	1000-1800	24	2401	625
<211>	25-750	16	1089	289
	775-950	20	1681	441
	1000-1800	24	2401	625
<100>	25-800	16	1089	289
	850-950	20	1681	441
	1000-1800	24	2401	625
<111>	25-750	16	1089	289
	775-950	20	1681	441
	1000-1800	24	2401	625

4. Considered lattice sites in the diamond structure

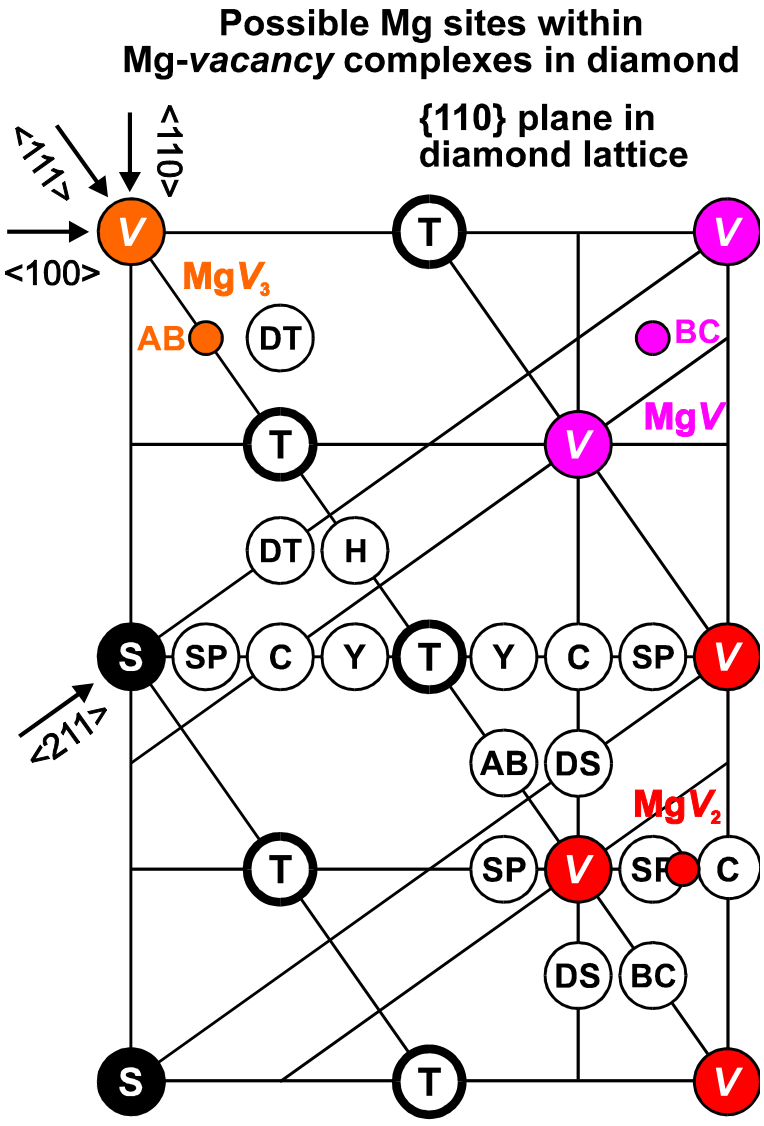

Figure S3. Positions of the substitutional and major interstitial sites in diamond. The interstitial sites shown are those of highest symmetry which are obtained by displacements from substitutional sites from the S position along <111>, i.e. bond-centered (BC), anti-bonding (AB), tetrahedral (T), and hexagonal (H); along <100>, i.e. <100>-split (SP) and the so-called "Yb" (Y, named after Yb) and "C" (C, named after its C_{2v} symmetry) sites; and along <110>, i.e. the <110>-split (DS). Possible structures for MgV, MgV_2, and MgV_3 complexes are shown in magenta, red, and orange, respectively. Please note, as is explained in the text, for this commonly chosen nomenclature, each complex contains one more vacancy than indicated by its name. In case of the MgV_3 complex, which contains 4 vacancies, three of them are out of the (110) plane that is shown in this figure.

Figure S3 shows the (110) plane of the diamond lattice with the positions of the substitutional (*S*) and major interstitial sites, as well as the established, predicted, or tentative structures of the most prominent Mg-vacancy complexes. Please note that, for historical reasons, the commonly chosen nomenclature for impurity-vacancy complexes in diamond originated in the nitrogen-vacancy complex. In that case, the N*V* complex consists of a substitutional N atom plus a lattice vacancy in nearest-neighbour position. It can be pictured as putting a N atom into a double vacancy, where it will fill up one of the vacant sites. In the case of Mg, the same procedure would lead to a most stable configuration which is different, i.e. the Mg atom occupying a position that is centered in between the two vacancies, the so-called split-vacancy configuration. Still the same nomenclature is used, for these structurally different configurations. In accordance, the complexes shown are:

Mg + 1V → Mg$_S$
Mg + 2V → MgV (BC site)
Mg + 3V → MgV_2 (interstitial site close to SP, i.e. <100> displacement from *S*)
Mg + 4V → MgV_3 (interstitial site close to AB, i.e. <111> displacement from *S*).

Theoretical predictions for their exact structure were so far only made [26] for the complexes Mg$_S$, MgV and MgV_2. For MgV_3 one tentatively expects trigonal symmetry with Mg located somewhere near AB sites, as is shown in the figure.

5. Theoretical emission patterns for substitutional and bond-center sites

<110>, <211>, <100>, and <111> β^- emission patterns from ^{27}Mg were calculated for a total of 245 different positions in the unit cell of the diamond lattice. For the calculations it was assumed that all possible orientations of the sites are populated with equal probability, which assumes that the surface orientation of the sample does not lead to the preferential occupation of certain orientations over others. In **Figure S4** we present the theoretical patterns that result from ^{27}Mg impurities on substitutional (*S*) and bond-center (BC) positions.

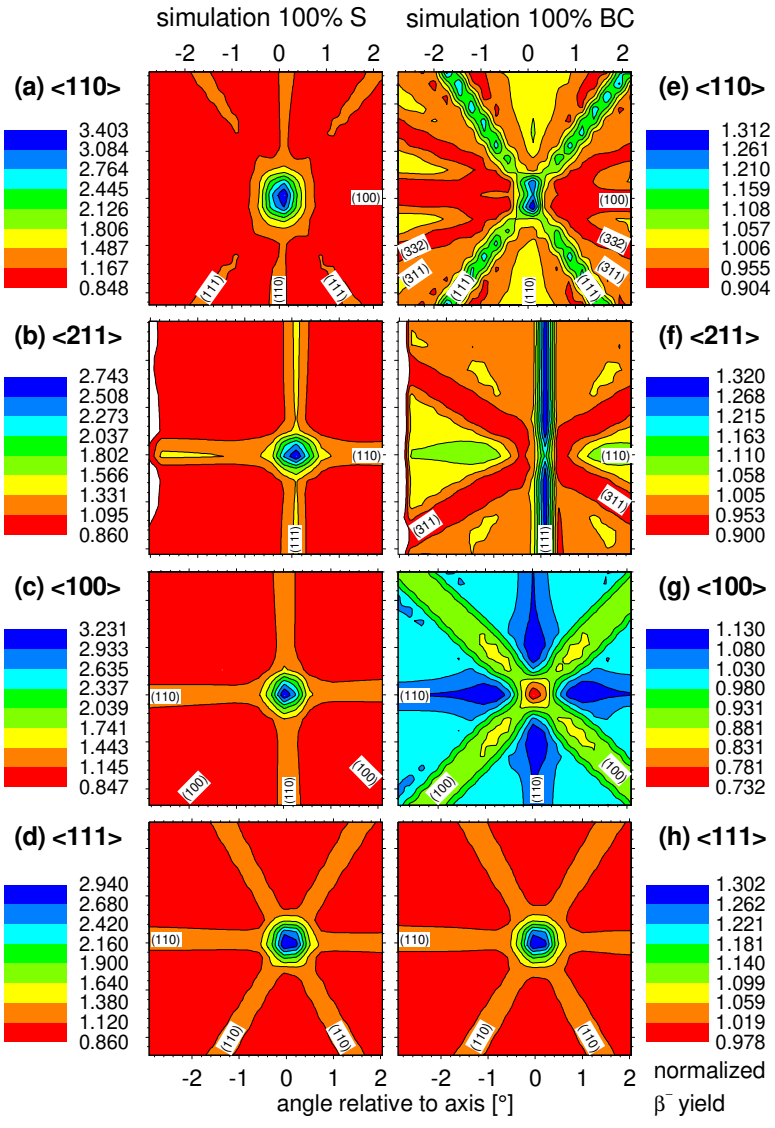

Figure S4. Theoretical β^- emission patterns around the major crystallographic directions of diamond for ^{27}Mg emitter atoms on the (a)-(d) ideal substitutional (*S*) and (e)-(h) bond-center (BC) sites. All patterns are displayed so as to reflect the orientation of the experimental patterns measured at 800°C in Figure 2 of the main paper, taking into account the angular resolution of the experimental data and the size and orientation of the detector pixels.

6. Peculiarity of <111> patterns

As can be seen from **Figure S4**, for the case of <111> patterns, the shape of the angular distributions resulting from ^{27}Mg on *S* and BC sites is very similar, although *S* sites show a much higher anisotropy than BC positions, 2.940 *vs* 1.302. Such cases are known in chi-square fitting as "linear dependencies", and the fit procedure cannot correctly assess the relative fractions on *S* and BC sites, since it optimizes chi square on marginal shape differences of the theoretical patterns. The reason for the similarity of the S and BC patterns is that for any particular <111> direction ¼ of the possible BC configurations in the diamond structure are aligned with this axis. These dominate the channeling effects, in contrast to the other ¾ configurations which are interstitial. We therefore had to exclude the <111> results from determining the fractions on *S* and BC sites. The theoretical patterns included for the <111> direction in **Figures 1h** and **2h** of the main paper are hence not those for the best fit results of that direction, but when the relative contribution from BC sites was fixed at the ratios that were derived from the analysis of the other three directions, i.e. $f(S) : f(\mathrm{BC}) = 26:74$ at RT as-implanted, and at 32:68 for 800°C implanted. As can be seen, **Figure 1h** and **2h** match the experimental results of **Figures 1d** and **2d** quite well; the <111> measurements are therefore compatible with the results from the other directions.

7. Comparison of Mg implantation conditions

In the current work, we have used two different ways to produce diamond samples doped with the stable isotope ^{24}Mg by means of ion implantation. On the one hand we used the Danfysik 1090 implanter of the KU Leuven Ion and Molecular Beam Laboratory (IMBL), which produces Mg^+ ions by means of heating the chemical compound $MgCl_2$ and ionizing the evaporated Mg atoms in a plasma. The production conditions for stable Mg beams at ISOLDE are the same as for radioactive beams, i.e. by means of 1.4 GeV proton-induced fragmentation of a Ti target, outdiffusion and resonant laser ionization, however, there are no stable contaminations with ^{24}Al since the only long-lived isotopes of Al are ^{26}Al ($t_{1/2}$=740000 y) and stable ^{27}Al.
In the following table we compare the ion production and beam characteristics of our stable and radioactive implantations, including also those of Refs [25,35] at the University of Leipzig used in previous studies of Mg in diamond (which were taken from the literature, hence not all details are known to us).

Table S3. Ion beam production characteristics for the diamond samples implanted with Mg in this work in comparison to those of Refs [25,35].

	KU Leuven	ISOLDE stable isotope	ISOLDE radioisotope	Ref. [25,35] (U Leipzig)
Ion source starting material	$MgCl_2$	1.4 GeV protons on Ti	1.4 GeV protons on Ti	Mg cathode
Mg extraction	evaporation by thermal heating	evaporation by thermal heating	evaporation by thermal heating	sputtering
Ion source	plasma	RILIS[1]	RILIS[1]	Cs sputter source
Produced ions	positive	positive	positive	negative
Beam energy [keV]	100	30	30	50
Mass resolving power $M/\Delta M$	~150-250	~2500	~2500	?
Implanted ion	$^{24}Mg^+$	$^{24}Mg^+$	$^{27}Mg^+$	$^{25}(^{24}Mg^1H)^-$
Collimator	Al, 200 µm edge length, 15 µm thick	Cu-Zn bronze tube, 1 mm ∅, 3 cm length	Cu-Zn bronze tube, 1 mm ∅, 3 cm length	~50 µm ∅
Implanted fluences [cm^{-2}]	5×10^9 5×10^{11} 5×10^{12} 5×10^{13}	1×10^{12}	$2.1\text{-}5.5\times10^{11}$ per EC pattern 1.1×10^{13} integral	1×10^{10} [25] 1×10^{11} [25] 1×10^{12} [25] 1×10^{13} [25] 1×10^{14} [25] 3×10^9 [35] 3×10^{10} [35] 3×10^{11} [35]

[1] RILIS = Resonant Ionization Laser Ion Source

8. Photoluminescence of RT *vs* 800°C ISOLDE ^{24}Mg implanted sample

A spectral analysis was also performed on a sample of "electronic grade" diamond especially implanted at ISOLDE for PL analysis with stable, non-radioactive ^{24}Mg. **Figure S5a** shows the high-resolution emission spectrum of a region implanted with 30 keV ^{24}Mg (1×10^{12} cm^{-2} fluence) at room temperature, followed by an 800°C, ~20 min annealing, during which time a different spot of the same sample was implanted at this higher temperature. Conversely, in **Figure S5b** the PL spectrum of the region implanted at the same fluence at 800°C temperature (without any additional annealing) is shown. In both cases, the typical emission spectrum of the Mg*V* center discussed above is clearly visible without additional radiation-induced PL features. This result suggests that similar Mg*V* formation can be obtained from the two implantation procedures. More importantly, **Figure S5b** certifies the presence of optically-active Mg*V* centers in the same configuration in which EC analysis was performed in Sect. 2 (**Figure 2**) of the main paper, thus providing an unambiguous link between the optical and structural analysis of the color center.

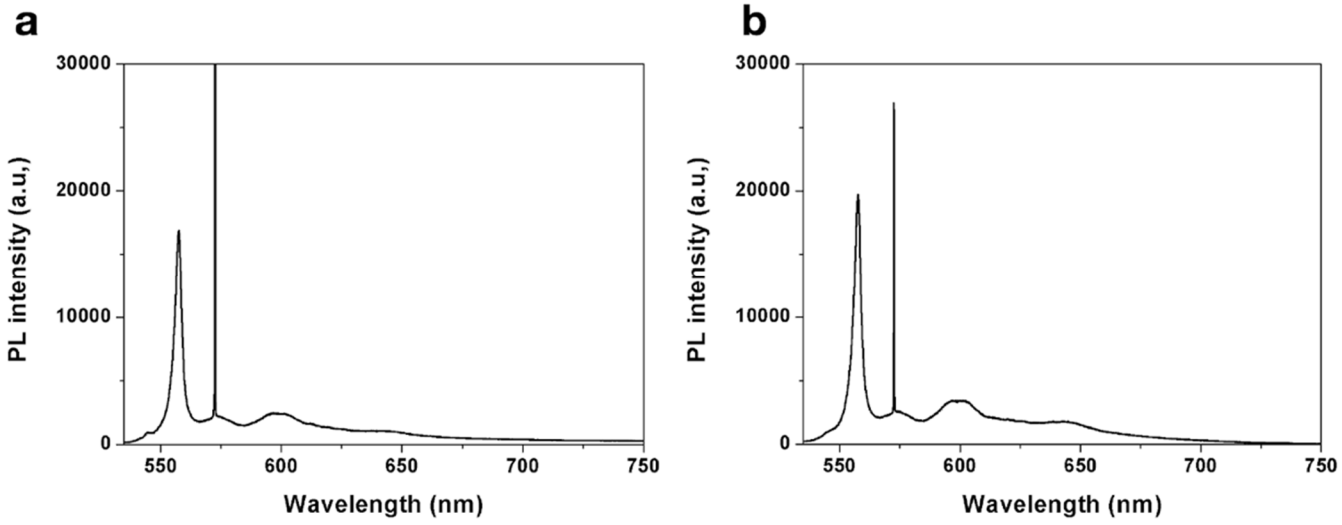

Figure S5. RT high-resolution spectra (532 nm excitation wavelength) of a SC "electronic grade" diamond sample implanted at CERN's ISOLDE facility with 30 keV ^{24}Mg (1×10^{12} cm^{-2} fluence): **a)** room temperature implantation, followed by 20 min 800°C annealing; **b)** implantation performed at 800°C.

9. Experimental details on optical characterization of Mg*V* centers

The experiments were performed using different photoluminescence setups. Firstly, a micro-Raman optical setup equipped with a Horiba Jobin Yvon HR800 spectrometer with 2 different gratings (1800 and 600 grooves/mm) and a cooled CCD detector was exploited for high-resolution (<0.1 nm) spectral analysis of Mg*V* ensembles. Two polarized lasers are mounted in the setup consisting of a 532 nm wavelength laser with an optical power of 250 mW and a 633 nm laser with an optical power of 20 mW. A set of objectives (10×, 20×, 50×, 100×) are mounted on an OlympusBx41 microscope which is arranged to operate in both reflection and transmission.

Spectral analysis at different emission wavelengths, confocal microscopy mapping and single-photon emission analysis were then performed by means of a custom fiber-coupled single-photon sensitive confocal microscope. In such systems a multimode optical fiber (core diameter ∅ = 50 μm) was used both as the pinhole of the confocal microscope and as the outcoupling medium for luminescence detection and analysis (**Figure S6**). Room temperature measurements were performed using a 100× air objective (Nikon CFI TU Plan Fluor, 0.9 N.A.), the sample was scanned over a 100×100×100 μm^3 closed-loop piezoelectric nanopositioner (Physik Instrumente P611.3s). Cryogenic measurements were performed by interfacing the aforementioned custom confocal microscope to a Montana S100 cryostation, equipped with a vacuum-compatible long-distance air objective (Zeiss EC Epiplan 100×, 0.85 N.A.). The sample was mounted on a three-axes open-loop nanopositioner. Luminescence maps and photon count rate were monitored by means of the QUDI open source software [47].

Second-order autocorrelation function measurements were performed by a Hanbury-Brown & Twiss interferometer implemented by connecting a fiber-fused balanced beam-splitter to two independent commercial silicon single-photon avalanche detectors (Excelitas SPCM AQRH, 250 cps dark counts). Time correlated single-photon counting (and the relative coincidence measurements) were performed exploiting an ID800 ID Quantique time tagger.

Spectral measurements were performed by connecting the optical output of the confocal microscope to a Horiba iHR320 monochromator, whose output port was fiber-coupled to a SPAD (spectral resolution: ~4 nm [24]). Measurements at varying laser wavelength were performed on the room-temperature PL setup by using both a discrete set of laser diodes and a supercontinuum laser (80 MHz NKT SuperK Fianum) with tunable emission wavelength [<10 nm bandwidth, **Figure 4c** of the main paper]. The spectral filtering performed using discrete laser diodes is reported in **Table S4**. The measurements in **Figure 4c** of the main paper were acquired with a 550 nm long-pass optical filtering.

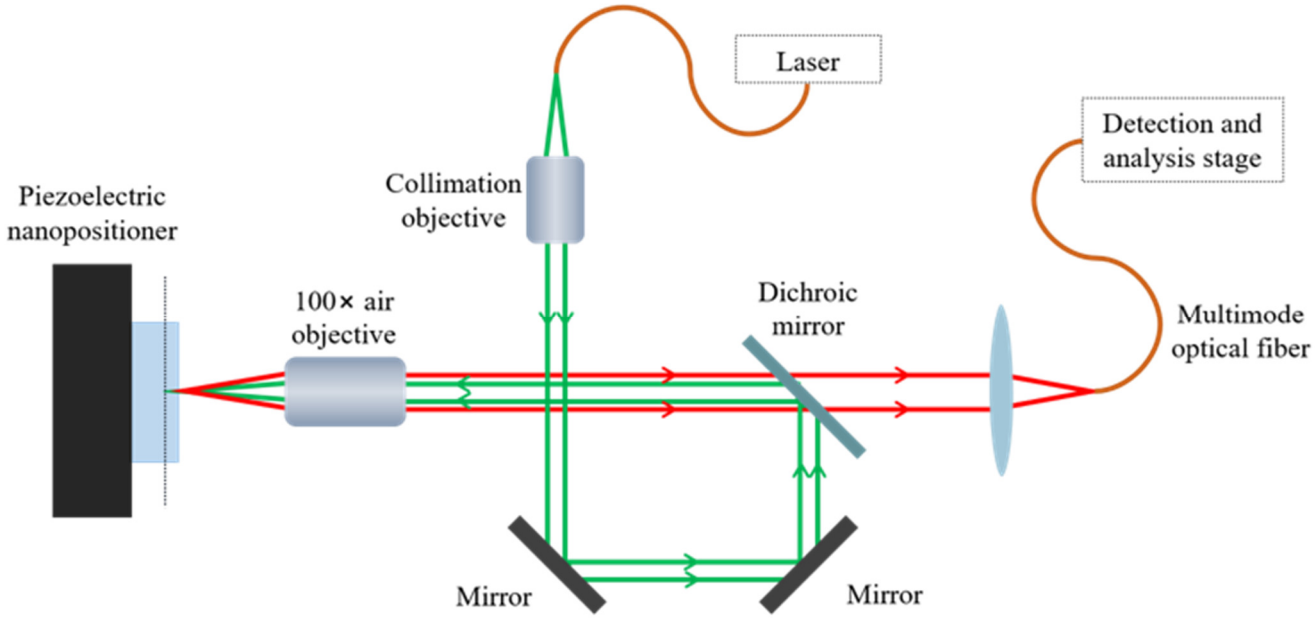

Figure S6. Setup adopted for single-photon-sensitive confocal microscopy experiments**.**

Table S4. List of the laser excitation wavelengths adopted for the characterization of Mg*V* centers, including details on the spectral filtering and the spectral position of the corresponding first-order Raman line.

Excitation source	**Confocal microscope**	**Spectral filtering**	**Raman line**
405 nm	Single-photon sensitive	505-700 nm spectral bandwith	428.1 nm
450 nm	Single-photon sensitive	505 nm long pass filter	478.7 nm
490.5 nm	Single-photon sensitive	505 nm long pass filter	524.8 nm
509.5 nm	Single-photon sensitive	525 nm long pass filter	546.5 nm
522 nm	Single-photon sensitive	550 nm long pass filter	561.0 nm
532 nm	Micro-Raman	Notch filter at 532 nm	572.8 nm